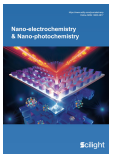
Scilight

Nano-electrochemistry & Nano-photochemistry

https://www.sciltp.com/journals/nenp



Article

Cross-Adsorbate Scaling, Interpretable Machine Learning, and Adsorption Trade-Offs across M–N_4–C Sites

Simin Li and Bo Shen *

Department of Materials Science and Engineering, City University of Hong Kong, 83 Tat Chee Avenue, Kowloon, Hong Kong SAR, China

* Correspondence: boshen@cityu.edu.hk

How To Cite: Li, S.; Shen, B. Cross-Adsorbate Scaling, Interpretable Machine Learning, and Adsorption Trade-Offs across M–N_4–C Sites. *Nano-electrochem. Nano-photochem*. **2026**, *2*(4), 24. https://doi.org/10.53941/nenp.2026.100024

Received: 11 September 2026
Revised: 21 October 2026
Accepted: 22 October 2026
Published: 3 November 2026

Abstract: Metal–nitrogen–carbon sites provide a chemically diverse platform for tuning adsorbate binding, yet the relationships among different C1 adsorption probes remain incompletely resolved. Here, density functional theory and interpretable machine learning are combined across a 35-metal M–N_4–C chemical space to examine *COOH, *CO, and *CHO adsorption as complementary probes. The adsorption landscapes are strongly adsorbate dependent, but *COOH and *CHO exhibit a cross-adsorbate scaling relation (R^2 = 0.919), consistent with similar metal-dependent stabilization across much of the series. In contrast, relationships involving *CO show larger residual variation. Gradient-boosting models evaluated by nested out-of-fold prediction recover descriptor-based signal for all three targets; *CO is predicted most accurately (R^2 = 0.851; MAE = 0.272 eV), whereas *COOH and *CHO show moderate predictability. Permutation importance, direct DFT correlations, and out-of-fold SHAP analysis identify d-electron count as a recurring organizer of *COOH and *CO adsorption and periodic group as a recurring organizer of *CO and *CHO adsorption. Robust regression highlights Os, Ru, and Re as pronounced *COOH–*CO scaling deviations, while Y departs strongly from the tighter *COOH–*CHO relation. Separate Pareto analyses highlight Y, Os, and Ti under different two-objective adsorption trade-offs. The combined analysis distinguishes shared adsorption trends from adsorbate-specific behavior and identifies chemically informative sites for subsequent mechanistic study.

Keywords: interpretable machine learning; single-atom catalysis; intermediate adsorption; adsorption-energy scaling

1. Introduction

Atomically dispersed metal centers coordinated by nitrogen in carbon provide a versatile platform for controlling the adsorption of carbon-containing intermediates [1]. Within the M–N_4–C motif, changing only the central metal can produce substantial shifts in electronic structure and binding strength while preserving a common first-shell coordination environment [2,3]. This combination makes the family useful for isolating periodic trends and for asking how far adsorption behavior can be organized by transferable chemical descriptors [4].

Computational studies of M–N_4–C materials often emphasize a single adsorbate or condense several energetic quantities into an overall performance descriptor [5–7]. Such approaches are valuable for screening, but they can obscure whether chemically distinct adsorbates respond similarly to changes in the metal center [8–10]. Cross-adsorbate comparisons are especially important because a strong scaling relation can simplify a chemical landscape while simultaneously constraining independent control of different binding events [11–13]. Conversely,

Copyright: © 2026 by the authors. This is an open access article under the terms and conditions of the Creative Commons Attribution (CC BY) license (https://creativecommons.org/licenses/by/4.0/).
Publisher's Note: Scilight stays neutral with regard to jurisdictional claims in published maps and institutional affiliations.

reproducible deviations from a dominant relation can reveal metal centers with unusual combinations of adsorption energies [14,15].

Machine learning offers a complementary route to organizing these trends [16]. For a compact chemical space, its most useful role is not merely to minimize prediction error [17], but to test whether pre-adsorption elemental and structural descriptors encode consistent chemical information [18,19]. Interpretation is demanding because descriptors such as atomic number, mass, period, group, radii, and local geometry are not independent [20]. Feature importance must therefore be considered alongside direct correlations with the calculated energies and directional out-of-fold attribution patterns [21]. This combined view can distinguish recurring organizing variables from isolated model rankings while avoiding causal claims that the data cannot establish [22].

The present study addresses four connected questions. First, how do *COOH, *CO, and *CHO adsorption energies co-vary across a common 35-metal M–N_4–C chemical family [23,24]? Second, are these adsorption targets organized by the same descriptors? Third, which metal centers deviate from the dominant cross-adsorbate relationships? Fourth, how do those deviations map onto distinct multi-objective adsorption trade-offs [25]? The three adsorbates are treated as complementary C1 probes rather than as a mandatory universal reaction sequence [26,27].

Density functional theory (DFT) establishes the adsorption-energy landscape, after which nested out-of-fold machine learning evaluates descriptor-based predictability [28]. Robust regression is used to distinguish dominant cross-adsorbate trends from unusual residuals, while separate Pareto analyses retain the chemical meaning of the three two-objective comparisons. Unlike conventional ML-assisted screening focused primarily on individual adsorption targets, the present study combines cross-adsorbate scaling, interpretable machine learning, scaling-deviation analysis, and Pareto trade-offs within a common M–N_4–C chemical space to identify adsorbate-dependent trends and chemically distinctive metal centers [29,30].

2. Materials and Methods

2.1. M–N_4–C Structures and DFT Calculations

A common M–N_4–C structural family was constructed for 35 metal centers spanning the 3d, 4d, 5d, and p-block series. The selected elements span diverse periodic groups, electronic configurations, and atomic sizes, enabling comparison of adsorption trends across a broad chemical space. A 3 × 3 × 1 M–N_4–C supercell was employed, with a vacuum layer of approximately 15 Å along the surface-normal direction to minimize interactions between periodic images. All atoms were allowed to relax during geometry optimization, while the simulation cell was kept fixed.

For the adsorption calculations, *COOH, *CO, and *CHO were initially placed above the central metal atom of the M–N_4 site, with the metal atom serving as the adsorption center. The adsorbate–metal geometries were subsequently optimized without fixing any atoms, and the optimized adsorption structures were used for the adsorption-energy calculations. For *COOH, when multiple initial adsorption configurations were considered, the lowest-energy optimized configuration was adopted for subsequent analysis.

Spin-polarized DFT calculations were performed with VASP 6.4.3 using projector-augmented-wave potentials and the PBE exchange–correlation functional [31–33]. The plane-wave cutoff was 420 eV, and Brillouin-zone sampling used a Γ-centered 1 × 1 × 1 mesh. The electronic and ionic settings were ISPIN = 2, ISYM = 0, PREC = Normal, ALGO = Fast, LREAL = Auto, LASPH = T, ADDGRID = T, ISMEAR = 0, SIGMA = 0.05 eV, EDIFF = 1×10^{-4} eV, IBRION = 2, ISIF = 2, and EDIFFG = −0.05 eV $Å^{-1}$. Hg did not retain the intended bare M–N_4 configuration and was not treated as a conventional member of that structural family in the chemical interpretation.

2.2. Adsorption-Energy Database

Adsorption energies for X = CO, CHO, and COOH were defined as:

$$E_{ads(*X)} = E_{slab+X} - E_{slab} - E_X$$

The reference energies were −14.803 eV for CO, −17.086 eV for CHO, and −24.464 eV for COOH. Negative adsorption energies denote stabilization relative to the separated M–N_4–C site and reference species.

2.3. Descriptors and Machine-Learning Workflow

Each metal site was represented by 11 pre-adsorption descriptors covering elemental identity, periodic position, electronic filling, size, and the local M–N_4 geometry: atomic number, atomic mass, period, group, d-electron count, electronegativity, atomic radius, covalent radius, metal height, mean M–N distance, and the standard deviation of M–N distances. The FULL representation comprised all 11 descriptors. Metal height

represents the out-of-plane displacement of the metal atom relative to the plane defined by its four coordinating nitrogen atoms. The mean M–N distance and its standard deviation characterize the average metal–nitrogen bond length and the corresponding local bond-length asymmetry, respectively. The COMPACT representation retained seven descriptors: electronegativity, covalent radius, periodic group, period, d-electron count, mean M–N distance, and the standard deviation of the M–N distances. The selected gradient-boosting models used the FULL set for *COOH, the COMPACT set for *CO, and the FULL set for *CHO. For each adsorbate, the FULL and COMPACT representations were compared under the same nested cross-validation protocol. When the nested out-of-fold MAE of the COMPACT representation was within 0.05 eV of that of the FULL representation, the simpler feature set was preferred to reduce descriptor redundancy [22].

Model assessment used nested cross-validation, separating model selection from held-out prediction. The outer evaluation used a five-fold cross-validation repeated over ten deterministic splits. Within each outer training partition, hyperparameters were selected using four-fold inner cross-validation with mean absolute error as the optimization metric. Headline MAE and R^2 values were calculated from aggregated out-of-fold predictions. A mean-prediction Dummy model provided the baseline. Supporting checks comprised 1000 target randomizations for each adsorbate, leave-one-out cross-validation, and 1000 bootstrap resamples for prediction stability. Permutation importance was normalized within each target. Out-of-fold SHAP [34,35] values were used to examine directionality: positive values shift a prediction toward higher adsorption energy, whereas negative values shift it toward lower adsorption energy [35]. Feature importance and attribution were interpreted as predictive associations rather than proof of causality.

2.4. Cross-Adsorbate Scaling Analysis

Pairwise linear scaling was evaluated for *COOH–*CO, *COOH–*CHO, and *CO–*CHO using the metals available for each pair. Ordinary least-squares fits quantified the dominant linear relationships through slopes and R^2 values; Pearson and Spearman coefficients described linear and rank association. Huber regression provided a robust comparison less sensitive to large residuals. Robust scaling deviations were identified from large standardized residuals that remained pronounced relative to both the ordinary least-squares and robust regression trends [36–40].

2.5. Pareto Analysis

Three two-objective Pareto analyses were performed independently: (A) strong *COOH stabilization versus weak *CO binding, representing easier *CO release; (B) simultaneous *COOH and *CHO stabilization; and (C) weak *CO binding versus strong *CHO stabilization. The fronts were not combined into a scalar score. A metal on one front, therefore, represents a trade-off for that specific chemical question and does not imply a universal activity ranking [41].

3. Results

3.1. Adsorbate-Dependent Chemistry across M–N_4–C Sites

The computational design holds the M–N_4–C coordination motif constant while varying the central element over 35 metals (Figure 1a,b). The resulting space includes 3d, 4d, 5d, and p-block centers and therefore samples a wide variation in d-electron filling, periodic position, atomic size, and local geometry. Hg does not retain the intended bare-site configuration and is consequently not interpreted as a conventional M–N_4 example. This structural exception does not obscure the broader chemical coverage of the metal series.

The adsorption-energy heatmap reveals a strongly adsorbate-dependent landscape (Figure 1c). COOH adsorption spans −3.872 to −0.244 eV, CO spans −2.948 to 0.0393 eV, and CHO spans −3.014 to 0.0803 eV. Broad distributions and different central tendencies are also evident in Figure S1. The ordering of metals differs among COOH, CO, and CHO, indicating that the three adsorption-energy datasets are not interchangeable.

3.2. Cross-Adsorbate Scaling Relationships

The clearest pairwise trend occurs between *COOH and *CHO (Figure 1d). For the 26 metals with both energies, the ordinary least-squares fit gives a slope of 0.956, $R^2 = 0.919$, Pearson $r = 0.959$, and Spearman $\rho = 0.915$.

Y is the most conspicuous departure from the *COOH–*CHO relation. Despite strong *COOH adsorption, its *CHO adsorption is substantially weaker than predicted by the dominant trend.

The full pairwise comparison shows weaker linear relationships whenever *CO is involved (Figure S7). *COOH–*CO uses 33 paired metals and gives a slope of 0.647, $R^2 = 0.593$, and Spearman $\rho = 0.822$. *CO–*CHO

uses 27 paired metals and gives a slope of 0.956, $R^2 = 0.605$, and Spearman $\rho = 0.832$. Both *CO-containing pairs show broader residual scatter than *COOH–*CHO.

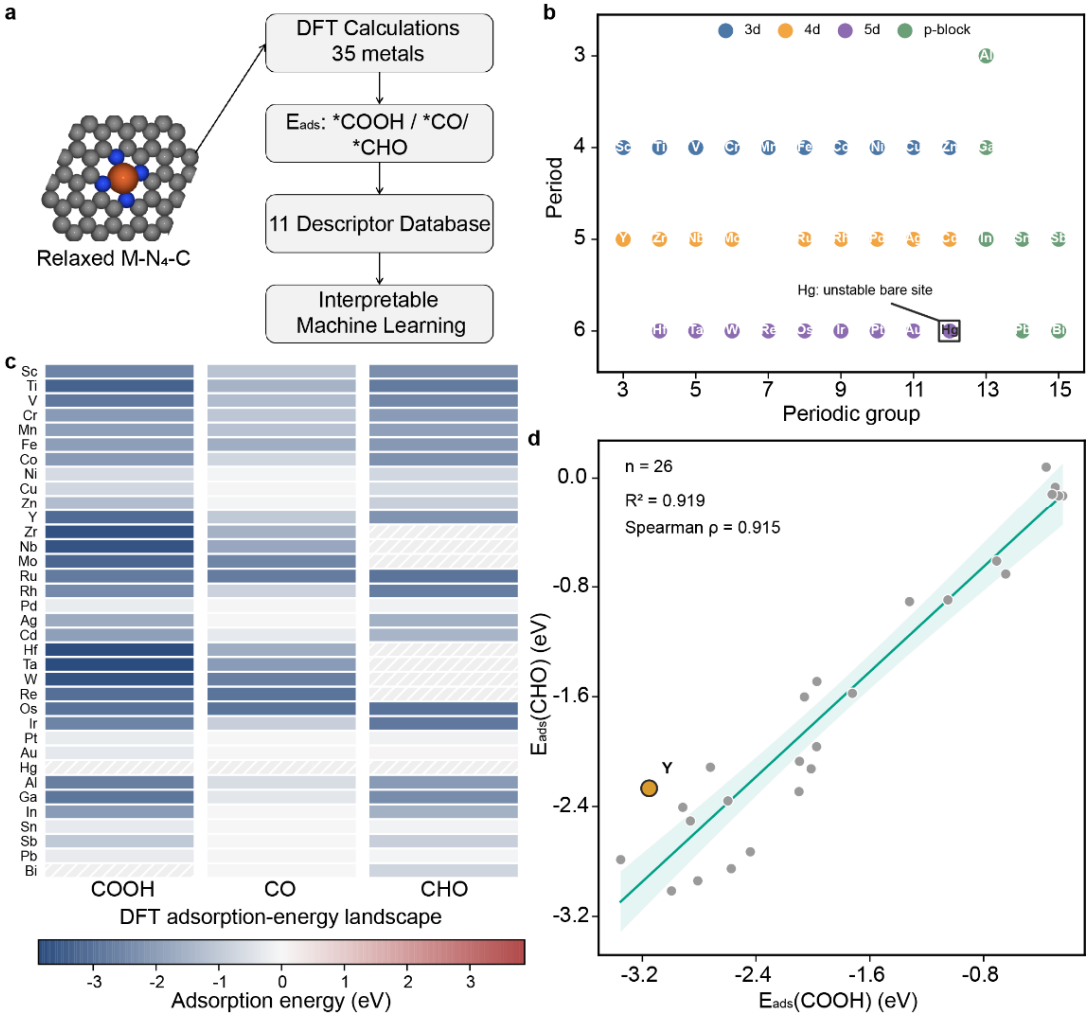


Figure 1. DFT adsorption landscape and cross-adsorbate scaling across M–N_4–C sites. (**a**) Conceptual workflow linking a common M–N_4–C structural family, DFT adsorption energies for *COOH, *CO, and *CHO, 11 pre-adsorption descriptors, and interpretable machine learning. (**b**) Thirty-five metal centers spanning the 3d, 4d, 5d, and p-block series. Hg does not retain the intended bare M–N_4 configuration and is not treated as a conventional M–N_4 example. (**c**) Heatmap of the adsorbate-dependent energy landscape; hatched cells indicate unavailable adsorbate–metal combinations. (**d**) *COOH–*CHO scaling for 26 paired metals. The relationship is the strongest of the three cross-adsorbate comparisons ($R^2 = 0.919$; Spearman $\rho = 0.915$), with Y highlighted as a major deviation.

3.3. Machine-Learning Prediction of Adsorption Energies

The selected gradient-boosting models outperform a mean-prediction baseline for all three adsorbates (Figure 2a). The selected feature representations are FULL for *COOH, COMPACT for *CO, and FULL for *CHO.

For *COOH, nested out-of-fold predictions give MAE = 0.533 eV and $R^2 = 0.616$ (Figure 2b). *CHO gives MAE = 0.538 eV and $R^2 = 0.506$ (Figure 2d). In both cases, sample-level dispersion around the parity line remains appreciable.

*CO is predicted most accurately, with MAE = 0.272 eV and $R^2 = 0.851$ (Figure 2c). Its out-of-fold predictions lie closer to the parity line than those for *COOH or *CHO.

The supporting validation checks are consistent with the nested out-of-fold results. In 1000 randomizations per adsorbate, shuffled targets yield markedly poorer cross-validated R^2 distributions than the observed targets, corresponding to an empirical significance of approximately $p = 0.001$ (Supplementary Figure S3). Leave-one-out predictions identify individual high-residual systems (Figure S4). Across 1000 bootstrap resamples, prediction intervals vary in width among metals (Figure S5).

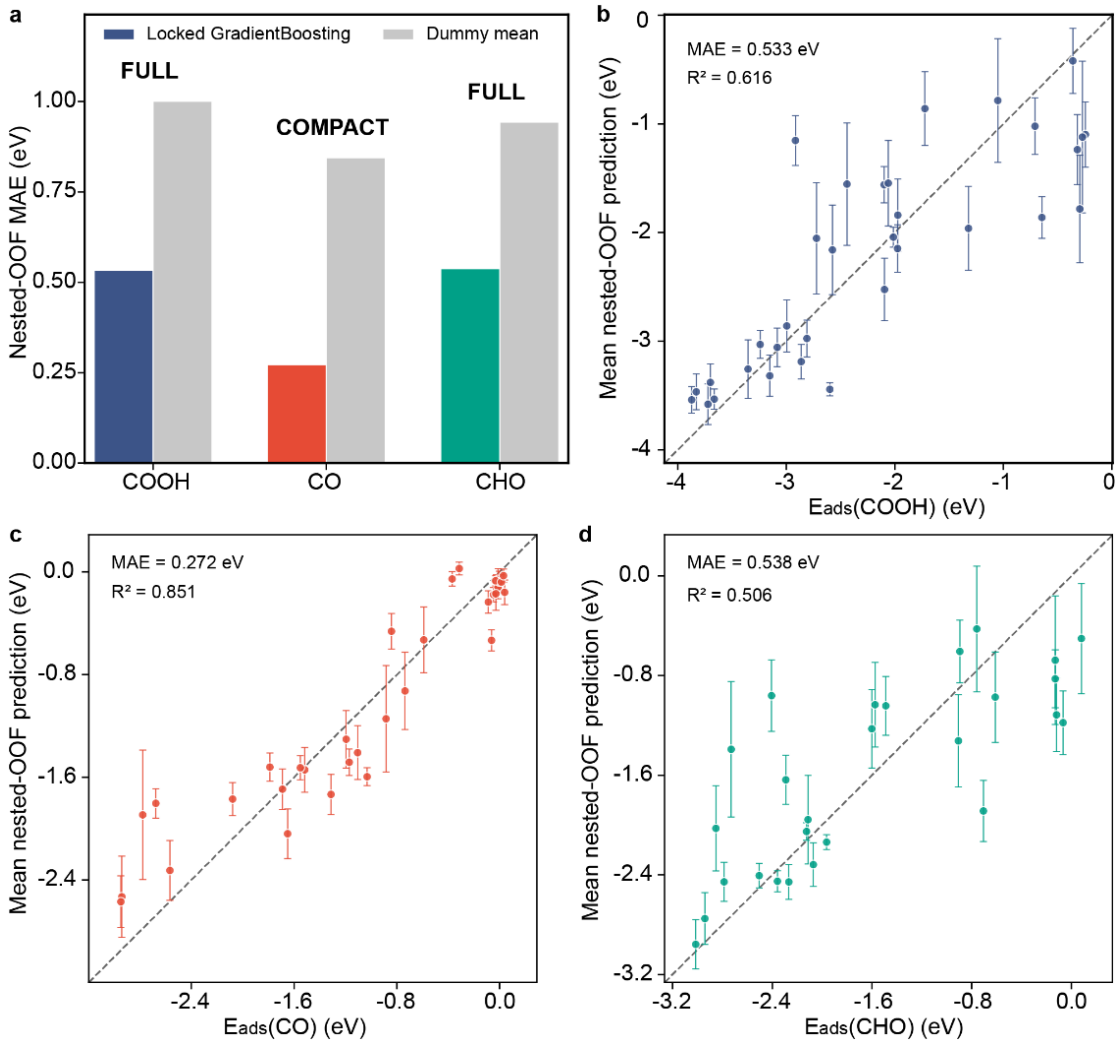


Figure 2. Out-of-fold machine-learning prediction of adsorption energies**.** (**a**) Nested out-of-fold MAE for the selected gradient-boosting models compared with a mean-prediction Dummy baseline. The selected representations are FULL for COOH, COMPACT for CO, and FULL for CHO. (**b**–**d**) Mean nested out-of-fold predictions versus DFT adsorption energies for b. COOH (MAE = 0.533 eV; R^2 = 0.616), (**c**) CO (MAE = 0.272 eV; R^2 = 0.851), and (**d**) CHO (MAE = 0.538 eV; R^2 = 0.506). Error bars show variation among held-out predictions, and dashed lines mark parity. As defined in Section 2.2, more negative adsorption energies correspond to stronger adsorption on both axes.

3.4. Interpretable Electronic and Periodic Descriptors

Permutation importance identifies a compact set of descriptors that recur across targets (Figure 3a). Bubble area represents the within-target normalized mean importance, so comparisons are most informative within each adsorbate and through repeated appearance across adsorbates. Two patterns stand out: d-electron count contributes prominently to *COOH and *CO prediction, whereas periodic group contributes prominently to *CO and *CHO prediction.

Direct DFT correlations show Spearman ρ = 0.768 between d-electron count and *COOH adsorption energy and ρ = 0.732 for *CO adsorption energy.

Periodic group gives Spearman ρ = 0.789 for *CO and ρ = 0.606 for *CHO. For *CO, the relationship is directly visible in Figure 3b (ρ = 0.789; $p = 3 \times 10^{-8}$), with adsorption becoming generally less negative toward later groups.

Several elemental and structural descriptor pairs have |Pearson r| > 0.90 (Figure S2), including correlations among atomic number, atomic mass, period, and local geometric quantities. Out-of-fold SHAP summaries (Figure S6) show directional contributions associated with d-electron count for *COOH and with periodic group for *CO and *CHO.

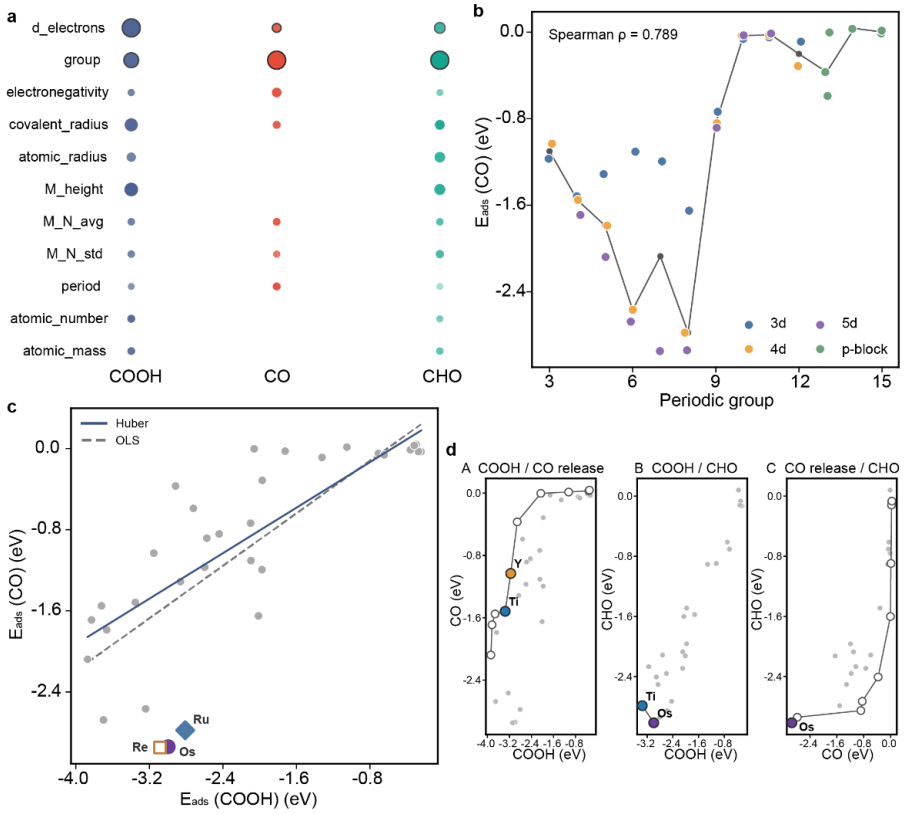


Figure 3. Interpretable descriptors, robust scaling deviations, and adsorption trade-offs. (**a**) Within-target normalized mean permutation importance for the 11 pre-adsorption descriptors; bubble area encodes normalized importance, and opacity encodes the fraction of positive importance estimates. (**b**) Direct DFT relationship between CO adsorption energy and periodic group (Spearman ρ = 0.789; $p = 3 \times 10^{-8}$). Colors denote metal series. (**c**) COOH–CO scaling with ordinary least-squares and Huber fits. Os, Ru, and Re are highlighted as robust scaling deviations with stronger CO binding than expected from the dominant trend. (**d**) Three separate Pareto questions: (**A**) strong COOH stabilization versus weak CO binding, (**B**) simultaneous COOH and CHO stabilization, and (**C**) weak CO binding versus strong CHO stabilization. Y, Os, and Ti are representative follow-up candidates identified by complementary analyses. The panels describe distinct trade-offs and do not constitute a universal ranking of activities.

3.5. Scaling Deviations and Multi-Objective Chemical Trade-Offs

Comparison of ordinary least-squares and Huber fits identifies Os, Ru, and Re as the most pronounced *COOH–*CO scaling deviations (Figure 3c). All three bind *CO substantially more strongly than predicted from their *COOH adsorption by the dominant relation.

Y provides a distinct deviation in the tighter *COOH–*CHO relation. With a background R^2 of 0.919, Y shows a substantially weaker *CHO adsorption energy than expected from its *COOH adsorption.

The three Pareto analyses yield different trade-off sets (Figure 3d). In panel A, which balances strong *COOH stabilization against weak *CO binding, Y and Ti lie on the highlighted front. In panel B, which considers simultaneous *COOH and *CHO stabilization, Ti and Os are highlighted. In panel C, which balances weak *CO binding against strong *CHO stabilization, Os is highlighted.

4. Discussion

The adsorption results show that a common M–N_4–C coordination motif does not impose a single metal ordering across different C1 probes. The particularly tight *COOH–*CHO relation, with a slope close to unity, indicates that these two oxygen-containing adsorbates respond similarly to metal substitution over much of the series. By contrast, the weaker *COOH–*CO and *CO–*CHO relationships leave substantially more residual variation. This distinction is important because adsorption-energy scaling can be useful for organizing a chemical space while also limiting the extent to which two intermediates can be tuned independently [11–15,29,30,36–40,42]. Here, the larger scatter involving *CO identifies a part of the adsorption landscape in which metal substitution has a more adsorbate-specific effect.

The machine-learning results describe a different aspect of the same dataset. *CO is the most accurately predicted target in held-out evaluation, whereas the strongest directly observed cross-adsorbate correlation occurs between *COOH and *CHO. These observations are not contradictory: cross-adsorbate scaling measures co-variation between two calculated energies, while the prediction task asks how much of one adsorption energy can be reconstructed from pre-adsorption elemental and structural descriptors. The distinction is useful for small catalyst datasets, where a high correlation between targets does not necessarily imply that both targets are equally predictable from the same feature set. The nested validation, target randomization, leave-one-out analysis, and bootstrap tests therefore serve complementary roles in assessing whether the descriptor signal is reproducible rather than a consequence of model selection [16–22,28,34,35].

The recurring importance of d-electron count and periodic group provides a compact chemical interpretation, but these quantities should be treated as organizing variables rather than isolated mechanistic descriptors. Both are correlated with other elemental properties, and several structural and elemental inputs are themselves strongly collinear. Consequently, permutation importance can be redistributed among related variables, while SHAP values describe the direction of a model association rather than a causal electronic mechanism. The agreement between the held-out interpretation and the direct DFT correlations nevertheless indicates that the periodic trends are present in the underlying adsorption energies and are not created solely by the regression model [20,34,35].

The scaling deviations and Pareto fronts provide two complementary ways to identify chemically unusual sites. Os, Ru, and Re depart from the dominant *COOH–*CO relation because they stabilize *CO more strongly than expected, whereas Y departs from the tighter *COOH–*CHO relation. The Pareto analysis adds a separate multi-objective view: Y, Os, and Ti emerge under different pairs of adsorption objectives rather than from a single combined score. This separation is deliberate. A deviation from a scaling relation is not, by itself, evidence of superior catalytic activity, and membership on one Pareto front does not establish optimality for a complete reaction network [37,41]. Instead, these metals are informative follow-up cases for testing why particular adsorption responses decouple from the dominant periodic trend.

Several limitations define the scope of these conclusions. The present comparison is based on adsorption energies within a common M–N_4–C structural family and does not include explicit electrode potential, solvent reorganization, kinetic barriers, or a complete reaction network. The chemical space is also compact, so descriptor correlations are strong and individual metals can have a noticeable influence on fitted relationships. Future calculations that resolve electronic structure and charge redistribution for the scaling outliers, together with potential- and solvation-dependent energetics and targeted mechanistic calculations, would be the most direct way to determine whether the identified deviations remain significant under reaction conditions. Within these limits, the current analysis is best viewed as a framework for selecting informative systems rather than as a universal activity ranking.

5. Conclusions

Across 35-metal M–N_4–C screening space, *COOH, *CO, and *CHO show distinct adsorption-energy landscapes. The strongest cross-adsorbate relation is *COOH–*CHO ($R^2 = 0.919$), whereas relationships involving *CO show greater residual variation. Interpretable gradient-boosting models recover descriptor-based signal for all three adsorbates, with *CO giving the best held-out performance ($R^2 = 0.851$; MAE = 0.272 eV). d-electron count and periodic group recur as useful organizing variables, although correlated descriptors preclude a simple causal interpretation. Robust regression identifies Os, Ru, and Re as *COOH–*CO scaling deviations and Y as the major *COOH–*CHO deviation, while separate Pareto analyses highlight Y, Os, and Ti under different adsorption trade-offs. Together, these results provide a systematic basis for selecting M–N_4–C sites for more detailed mechanistic study.

Supplementary Materials

The additional data and information can be downloaded at: https://media.sciltp.com/articles/others/2611031038599177/NENP-26090096-SI.pdf. Figure S1. Adsorption-energy distributions of COOH, CO, and CHO across M–N_4–C sites. Figure S2. Pearson correlation matrix of the 11 candidate descriptors. Figure S3. Target-randomization tests for the adsorption-energy prediction models. Figure S4. Leave-one-out predictions and residual diagnostics for COOH, CO, and CHO. Figure S5. Bootstrap prediction stability of the adsorption-energy models. Figure S6. Out-of-fold SHAP summaries for the selected models. Figure S7. Pairwise scaling relationships among COOH, CO, and CHO adsorption energies.

Author Contributions

S.L. conceived the project, designed the computational study, performed the calculations and data analysis, and wrote the original draft. B.S. supervised the research and contributed to interpretation, review, and editing. All authors have read and agreed to the submitted version of the manuscript.

Funding

This work was financially supported by the National Key R&D Program of China (2025YFA1511200), and the Small Scale Projects of City University of Hong Kong (Project No. 7020204). B.S. acknowledges support through the City University of Hong Kong start-up grant (Project No. 9382005).

Data Availability Statement

Data are contained within the article.

Conflicts of Interest

The authors declare no conflict of interest.

Use of AI and AI-Assisted Technologies

During the preparation of this work, the authors used ChatGPT to check grammar and improve language clarity. After using this tool, the authors reviewed and edited the content as needed and take full responsibility for the published article.

References

1. Qiao, B.; Wang, A.; Yang, X.; et al. Single-atom catalysis of CO oxidation using Pt1/FeOx. *Nat. Chem.* **2011**, *3*, 634–641. https://doi.org/10.1038/nchem.1095.
2. Yang, X.F.; Wang, A.; Qiao, B.; et al. Single-Atom Catalysts: A New Frontier in Heterogeneous Catalysis. *Accounts Chem. Res.* **2013**, *46*, 1740–1748. https://doi.org/10.1021/ar300361m.
3. Liu, J. Catalysis by Supported Single Metal Atoms. *ACS Catal.* **2016**, *7*, 34–59.
4. Xie, L.; Liu, Y.; Li, S.; et al. Phase and facet engineering for nanoscale catalyst discovery in electrochemical CO_2 reduction. *Nat. Synth.* **2026**, *5*, 489–505. https://doi.org/10.1038/s44160-026-01025-4.
5. Wang, A.; Li, J.; Zhang, T. Heterogeneous single-atom catalysis. *Nat. Rev. Chem.* **2018**, *2*, 65–81.
6. Yang, H.; Lin, Q.; Zhang, C.; et al. Carbon dioxide electroreduction on single-atom nickel decorated carbon membranes with industry compatible current densities. *Nat. Commun.* **2020**, *11*, 593.
7. Fauzi, A.; Chen, X.; Zhao, H.; et al. Recent progress of M-N-C single atom electrocatalysts for carbon dioxide reduction reaction. *Next Energy* **2023**, *1*, 100045. https://doi.org/10.1016/j.nxener.2023.100045.
8. Back, S.; Lim, J.; Kim, N.Y.; et al. Single-atom catalysts for CO_2 electroreduction with significant activity and selectivity improvements. *Chem. Sci.* **2017**, *8*, 1090–1096. https://doi.org/10.1039/c6sc03911a.
9. Zhang, J.; Cai, W.; Hu, F.X.; et al. Recent advances in single atom catalysts for the electrochemical carbon dioxide reduction reaction. *Chem. Sci.* **2021**, *12*, 6800–6819. https://doi.org/10.1039/d1sc01375k.
10. Wang, G.; Li, S.; Yu, C.; et al. High-Index-Faceted Cu Nanoparticles in Ag–Cu Tandem Catalysts for Selective CO_2 Electroreduction. *ACS Nanosci. Au* **2026**, *6*, 1029–1036. https://doi.org/10.1021/acsnanoscienceau.6c00129.
11. Cui, X.; An, W.; Liu, X.; et al. C_2N-graphene supported single-atom catalysts for CO_2 electrochemical reduction reaction: Mechanistic insight and catalyst screening. *Nanoscale* **2018**, *10*, 15262–15272. https://doi.org/10.1039/c8nr04961k.
12. Yang, Y.T.; Li, J.; Zhang, C.; et al. Theoretical Insights into Nitrogen-Doped Graphene-Supported Fe, Co, and Ni as Single-Atom Catalysts for CO_2 Reduction Reaction. *J. Phys. Chem. C* **2022**, *126*, 4338–4346. https://doi.org/10.1021/acs.jpcc.1c09740.
13. Qin, C.; Li, T.; Masakorala, G.; et al. Boosting CO_2-to-C_2H_4 electrocatalysis on Cu_2O with waste-derived porous carbon from coconut shells. *Chem. Commun.* **2026**, *62*, 10482–10486. https://doi.org/10.1039/d6cc01782g.
14. Wang, Q.; Liu, K.; Hu, K.; et al. Attenuating metal-substrate conjugation in atomically dispersed nickel catalysts for electroreduction of CO_2 to CO. *Nat. Commun.* **2022**, *13*, 6082. https://doi.org/10.1038/s41467-022-33692-0.
15. Wang, J.; Huang, Y.C.; Wang, Y.; et al. Atomically Dispersed Metal–Nitrogen–Carbon Catalysts with d-Orbital Electronic Configuration-Dependent Selectivity for Electrochemical CO_2-to-CO Reduction. *ACS Catal.* **2023**, *13*, 2374–2385.
16. Butler, K.T.; Davies, D.W.; Cartwright, H.; et al. Machine learning for molecular and materials science. *Nature* **2018**, *559*, 547–555. https://doi.org/10.1038/s41586-018-0337-2.
17. Palkovits, S. A Primer about Machine Learning in Catalysis—A Tutorial with Code. *ChemCatChem* **2020**, *12*, 3995–4008.

18. Shi, Y.; Liang, Z. Machine learning accelerates the screening of single-atom catalysts towards CO_2 electroreduction. *Appl. Catal. A Gen.* **2024**, *676*, 119674. https://doi.org/10.1016/j.apcata.2024.119674.
19. Tran, K.; Ulissi, Z.W. Active learning across intermetallics to guide discovery of electrocatalysts for CO_2 reduction and H2 evolution. *Nat. Catal.* **2018**, *1*, 696–703. https://doi.org/10.1038/s41929-018-0142-1.
20. Esterhuizen, J.A.; Goldsmith, B.R.; Linic, S. Interpretable machine learning for knowledge generation in heterogeneous catalysis. *Nat. Catal.* **2022**, *5*, 175–184. https://doi.org/10.1038/s41929-022-00744-z.
21. Zhong, M.; Tran, K.; Min, Y.; et al. Accelerated discovery of CO_2 electrocatalysts using active machine learning. *Nature* **2020**, *581*, 178–183. https://doi.org/10.1038/s41586-020-2242-8.
22. Varma, S.; Simon, R.M. Bias in error estimation when using cross-validation for model selection. *BMC Bioinform.* **2006**, *7*, 91. https://doi.org/10.1186/1471-2105-7-91.
23. Nguyen, T.N.; Salehi, M.; Le, Q.V.; et al. Fundamentals of Electrochemical CO_2 Reduction on Single-Metal-Atom Catalysts. *ACS Catal.* **2020**, *10*, 10068–10095. https://doi.org/10.1021/acscatal.0c02643.
24. Yao, L.; Ye, S.; Li, Z.; et al. Electrochemical nitrate-to-ammonia conversion over a broad concentration range via a hollow Co_3O_4/CuO catalyst. *Green Chem.* **2026**, *28*, 7827–7835. https://doi.org/10.1039/d6gc00484a.
25. Wang, L.; Shen, B.; He, Z.D.; et al. Universal framework for efficient estimation of stability in multi-principal element alloys. *Nat. Commun.* **2026**, *17*, 3093. https://doi.org/10.1038/s41467-026-69585-9.
26. Su, X.; Yang, X.; Huang, Y.; et al. Single-Atom Catalysis toward Efficient CO_2 Conversion to CO and Formate Products. *Accounts Chem. Res.* **2018**, *52*, 656–664. https://doi.org/10.1021/acs.accounts.8b00478.
27. Hansen, H.A.; Varley, J.B.; Peterson, A.A.; et al. Understanding Trends in the Electrocatalytic Activity of Metals and Enzymes for CO_2 Reduction to CO. *J Phys. Chem. Lett.* **2013**, *4*, 388–392.
28. Huang, Y.; Wang, J.; Hu, H.; et al. Heteroatom-doped M-N_4-C Single-atom catalysts towards electrochemical reactions of CO_2: A machine learning-assisted DFT study. *Mol. Catal.* **2025**, *572*, 114793. https://doi.org/10.1016/j.mcat.2024.114793.
29. Zhang, S.; Fan, Q.; Xia, R.; et al. CO_2 Reduction: From Homogeneous to Heterogeneous Electrocatalysis. *Accounts Chem. Res.* **2020**, *53*, 255–264. https://doi.org/10.1021/acs.accounts.9b00496.
30. Kolb, M.J.; Loffreda, D.; Sautet, P.; et al. Structure-sensitive scaling relations among carbon-containing species and their possible impact on CO_2 electroreduction. *J. Catal.* **2021**, *395*, 136–142. https://doi.org/10.1016/j.jcat.2020.12.026.
31. Kresse, G.; Furthmüller, J. Efficient iterative schemes for ab initio total-energy calculations using a plane-wave basis set. *Phys. Rev. B* **1996**, *54*, 11169–11186. https://doi.org/10.1103/physrevb.54.11169.
32. Kresse, G.; Joubert, D. From ultrasoft pseudopotentials to the projector augmented-wave method. *Phys. Rev. B* **1999**, *59*, 1758–1775. https://doi.org/10.1103/physrevb.59.1758.
33. Perdew, J.P.; Burke, K.; Ernzerhof, M. Generalized Gradient Approximation Made Simple. *Phys. Rev. Lett.* **1996**, *77*, 3865–3868. https://doi.org/10.1103/physrevlett.77.3865.
34. Ji, Z.; Chen, A.; Sun, J.; et al. Elucidating the fundamental governing principles of CO_2 reduction on single-atom catalysts through interpretable machine learning. *J. Mater. Chem. A* **2026**, *14*, 14612–14622. https://doi.org/10.1039/d5ta10584f.
35. Lundberg, S.M.; Erion, G.; Chen, H.; et al. From local explanations to global understanding with explainable AI for trees. *Nat. Mach. Intell.* **2020**, *2*, 56–67. https://doi.org/10.1038/s42256-019-0138-9.
36. Montemore, M.M.; Medlin, J.W. Scaling relations between adsorption energies for computational screening and design of catalysts. *Catal. Sci. Technol.* **2014**, *4*, 3748–3761. https://doi.org/10.1039/c4cy00335g.
37. Govindarajan, N.; García-Lastra, J.M.; Meijer, E.J.; et al. Does the breaking of adsorption-energy scaling relations guarantee enhanced electrocatalysis? *Curr. Opin. Electrochem.* **2018**, *8*, 110–117.
38. Calle-Vallejo, F.; Loffreda, D.; Koper, M.T.M.; et al. Introducing structural sensitivity into adsorption–energy scaling relations by means of coordination numbers. *Nat. Chem.* **2015**, *7*, 403–410. https://doi.org/10.1038/nchem.2226.
39. Abild-Pedersen, F.; Greeley, J.; Studt, F.; et al. Scaling Properties of Adsorption Energies for Hydrogen-Containing Molecules on Transition-Metal Surfaces. *Phys. Rev. Lett.* **2007**, *99*, 016105. https://doi.org/10.1103/physrevlett.99.016105.
40. Greeley, J. Theoretical Heterogeneous Catalysis: Scaling Relationships and Computational Catalyst Design. *Annu. Rev. Chem. Biomol. Eng.* **2016**, *7*, 605–635. https://doi.org/10.1146/annurev-chembioeng-080615-034413.
41. Bennett, J.A.; Orouji, N.; Khan, M.; et al. Autonomous reaction Pareto-front mapping with a self-driving catalysis laboratory. *Nat. Chem. Eng.* **2024**, *1*, 240–250. https://doi.org/10.1038/s44286-024-00033-5.
42. Zhang, Z.; Xing, Z.; Gou, X.; et al. Operando electrochemiluminescence imaging of intermediate evolution and kinetics in electrocatalytic nitrate reduction. *Nat. Commun.* **2026**, *17*, 10552.